Nanoscale

PAPER

View Article Online
View Journal | View Issue

Check for updates

Cite this: *Nanoscale*, 2025, **17**, 8563

Comparative electromagnetic shielding performance of $Ti_3C_2T_x$-PVA composites in various structural forms: compact films, hydrogels, and aerogels†

Shabbir Madad Naqvi,[a] Tufail Hassan,[a] Aamir Iqbal,[a] Shakir Zaman,[a] Sooyeong Cho,[a] Noushad Hussain,[a] Xiangmeng Kong,[a] Zubair Khalid,[a] Zhiwang Hao[a] and Chong Min Koo *[a,b]

Received 31st January 2025,
Accepted 26th February 2025

DOI: 10.1039/d5nr00450k

rsc.li/nanoscale

The structural design of light-weight MXene–polymer composites has attracted significant interest for enhancing both electromagnetic interference (EMI) shielding performance and mechanical strength, which are critical for practical applications. However, a systematic understanding of how various structural configurations of MXene composites affect EMI shielding is lacking. In this study, light-weight $Ti_3C_2T_x$-PVA composites were fabricated in three structural forms, hydrogel, aerogel, and compact film, while varying the $Ti_3C_2T_x$ areal density (14 to 20 mg cm^{-2}) to elucidate the role of structural design in X-band EMI shielding and mechanical properties. The EMI shielding performance depends on the structural configuration and areal density of the MXene in $Ti_3C_2T_x$-PVA composites. The shielding effectiveness increases with increasing $Ti_3C_2T_x$ content in each configuration. At a fixed $Ti_3C_2T_x$ areal density of 0.02 g cm^{-2}, the $Ti_3C_2T_x$-PVA hydrogel demonstrated the highest shielding effectiveness (SE = 70 dB at 10 GHz), attributed to strong dipole polarization and efficient ionic conduction behavior, followed by the compact film (40 dB) and then the aerogel (21 dB). Notably, the aerogel achieved the highest absorption coefficient (A = 0.89) due to the improved impedance matching and pronounced internal reflections, whereas the hydrogel and compact film exhibited reflection-dominated shielding. Furthermore, the incorporation of PVA polymer molecules into $Ti_3C_2T_x$ MXenes significantly enhanced their mechanical properties across all configurations: the hydrogel achieved high stretchability (636%), the aerogel displayed superior compressive strength (0.215 MPa), and the compact film reached a tensile strength of 56 MPa, each surpassing the performance of its pristine $Ti_3C_2T_x$ MXene counterpart. Overall, tailoring the structural configuration into a hydrogel, aerogel, or compact film offers versatile routes for optimizing both EMI attenuation and mechanical performance of MXene–polymer composites.

Introduction

Rapid advances in mobile electronics and telecommunication technologies have led to widespread electromagnetic interference (EMI) issues such as device malfunctions, signal distortion, data loss, and even system failures in highly integrated compact electronic systems.[1–3] Traditionally, highly conductive metals such as aluminum, copper, and silver have been used for EMI shielding due to their high electrical conductivity and resulting strong shielding capabilities.[4–6] However, the related high density and challenges in applying thin uniform coatings on unevenly shaped devices hinder their use as light-weight shielding materials. On the other hand, light-weight conductive carbon-based materials such as graphene and carbon nanotubes require relatively high thickness and filler loadings to achieve satisfactory EMI shielding performance due to their low electrical conductivity.[7–11]

Recently, MXenes, a large family of two-dimentional (2D) transition metal carbides, nitrides, and carbonitrides, have emerged as promising light-weight shielding materials. MXenes offer excellent metallic conductivity (exceeding 24 000 S cm^{-1}),[12] tunable composition,[13] low apparent density, and outstanding solution processability.[14] This was first demonstrated in 2016, when the $Ti_3C_2T_x$ MXene exhibited remarkable

---

[a] *School of Advanced Materials Science and Engineering, Sungkyunkwan University, Seobu-ro 2066, Jangan-gu, Suwon-si, Gyeonggi-do, 16419, Republic of Korea. E-mail: chongminkoo@skku.edu*

[b] *School of Chemical Engineering, Sungkyunkwan University, Seobu-ro 2066, Jangan-gu, Suwon-si, Gyeonggi-do, 16419, Republic of Korea*

† Electronic supplementary information (ESI) available. See DOI: **https://doi.org/10.1039/d5nr00450k**

EMI shielding effectiveness (SE), achieving 92 dB at a thickness of 45 μm.[15] Furthermore, a 40 μm thick Ti_3CNT_x MXene film achieved an EMI SE of 116 dB, the highest value reported for any synthetic material.[16] These findings highlight the potential of MXenes to outperform metals and carbon-based materials in EMI shielding at comparable thicknesses.

Despite their promising shielding performance, MXenes face challenges such as limited mechanical strength, dimensional stability, and long-term oxidation resistance, which are essential for practical applications. To address these challenges, interest has been growing in MXene-based polymer composites, which combine the excellent shielding properties of MXenes with the mechanical strength and structural stability of polymers.

The abundant surface terminal groups of MXenes, such as hydroxyl groups, provide easy solution processability, enabling the development of MXene–polymer composites in various structural configurations, including compact systems (films), porous structures (aerogels), and ionic species inclusions (hydrogels).[17] These configurations have been investigated for their EMI shielding capabilities, and several studies have shown significant performance.

For instance, the first report of a $Ti_3C_2T_x$ MXene compact composite film combined with sodium alginate (SA) achieved an EMI SE of 57 dB at a thickness of 8 μm.[15] Since then, MXene composite films have been incorporated into a wide range of natural and synthetic polymers, including non-conductive materials such as polyethylene (PE), polymethyl methacrylate (PMMA), cellulose nanofibers (CNFs), polyvinyl alcohol (PVA), polyurethane (PU), polycarbonate (PC), polyvinylidene fluoride (PVDF), polyimide (PI), and polystyrene (PS), as well as conductive polymers like polypyrrole (PPy), polyaniline (PANI), and poly(3,4-ethylenedioxythiophene) polystyrene sulfonate (PEDOT:PSS). These composite films have exhibited EMI SE ranging from 45 to 90 dB at thicknesses between 11 and 400 μm.[18–27] Porous structures, such as aerogels, benefit from multiple interphase interfaces, which promote multiple reflections and internal scattering of EM waves, indicating them as promising light-weight materials for EMI shielding. PVA-based $Ti_3C_2T_x$ aerogels exhibited EMI SE values of 26–33 dB at thicknesses of 3.4–3.9 mm, whereas $Ti_3C_2T_x$-polyamide aerogels achieved a much higher SE of 80 dB at 210 μm.[28,29] Similarly, $Ti_3C_2T_x$-SA aerogels reached an EMI SE of 70 dB at 2 mm, and $Ti_3C_2T_x$-PU foam exhibited an EMI SE of 72 dB at the same thickness.[23,30] Moreover, $Ti_3C_2T_x$ and water-soluble polymers can be effectively integrated into soft composite hydrogels; polar water molecules and mobile ions in the hydrogel configuration can significantly improve the attenuation of EM waves through polarization loss.[31] For example, $Ti_3C_2T_x$-PEDOT:PSS hydrogels achieved an EMI SE of 51.7 dB at a thickness of approximately 0.3 mm,[32] and $Ti_3C_2T_x$-PVA hydrogels exhibited an EMI SE of 31 dB at 1 mm thickness,[33] with another reported material reaching an EMI SE of 48.6 dB at 1.5 mm.[34]

Despite these advances, a comprehensive study of shielding mechanisms across different structural types, such as hydrogels, aerogels, and compact films, remains a gap in the literature. A thorough exploration of these variations is essential for gaining a deeper understanding of how structural configuration affects the EMI shielding performance.

Therefore, this study investigates the EMI shielding performance of $Ti_3C_2T_x$-PVA composites in three distinct structural configurations: hydrogels, aerogels, and compact films. High-crystallinity $Ti_3C_2T_x$ is used as a highly conductive MXene filler, and water-soluble PVA is chosen as the polymer matrix due to its excellent compatibility with the hydrophilic surface of $Ti_3C_2T_x$, enabling fabrication of homogeneous MXene–polymer composites in three structural configurations. By exploring the influence of structural configuration on EMI SE, this study provides a deeper understanding of how the arrangement and concentration of MXenes in polymer matrices can influence the EMI shielding performance. This study highlights the critical role of structural configuration in optimizing the EMI shielding performance of $Ti_3C_2T_x$-PVA composites.

Results and discussion

Preparation of hydrogels, aerogels, and compact films

To investigate the effects of structural configurations on EMI shielding, $Ti_3C_2T_x$-PVA composites were fabricated as hydrogels, aerogels, and compact films (Fig. 1a). Initially, the $Ti_3C_2T_x$ MXene was synthesized *via* selective etching of Al from highly crystalline Ti_3AlC_2 MAX phase crystals (Fig. S1a†) using the modified minimally intensive layer delamination (MILD) etching method.[35] Successful etching was confirmed using the X-ray diffraction (XRD) pattern, where the (00*l*) peak shifted from 8.57° to 7.26°, indicating an increase in *d*-spacing from 1.03 nm to 1.22 nm (Fig. 1b, red spectra). The absence of characteristic Ti_3AlC_2 MAX peaks further confirmed complete removal of Al from Ti_3AlC_2 and successful synthesis of the $Ti_3C_2T_x$ MXene.[36] Transmission electron microscopy (TEM) images and the corresponding selected area electron diffraction (SAED) patterns (Fig. 1c) revealed a single $Ti_3C_2T_x$ MXene sheet with a highly crystalline hexagonal lattice structure. Scanning electron microscopy (SEM) images also confirmed the well-delaminated morphology of the MXene sheet, which appeared to be partially electron transparent (Fig. S1b†). A characteristic peak at 760 nm in the UV-visible spectrum (Fig. 1d) and the bright greenish color of the $Ti_3C_2T_x$ dispersion (inset, Fig. 1d) further support the successful synthesis and delamination of the high-crystallinity $Ti_3C_2T_x$ MXene.

Due to the excellent dispersibility of $Ti_3C_2T_x$ and the solubility of PVA in deionized water, a homogeneous $Ti_3C_2T_x$-PVA aqueous solution formed readily, enabling the fabrication of hydrogels, aerogels, and compact films at various $Ti_3C_2T_x$ areal densities (14–20 mg cm^{-2}). $Ti_3C_2T_x$-PVA hydrogels were fabricated by adding sodium tetraborate to the $Ti_3C_2T_x$-PVA solution. The crosslinking process occurs in two stages. In the first stage, the tetrahydroxy borate anion reacts with a diol group on the PVA chain, forming a monodiol complex. In the second stage,

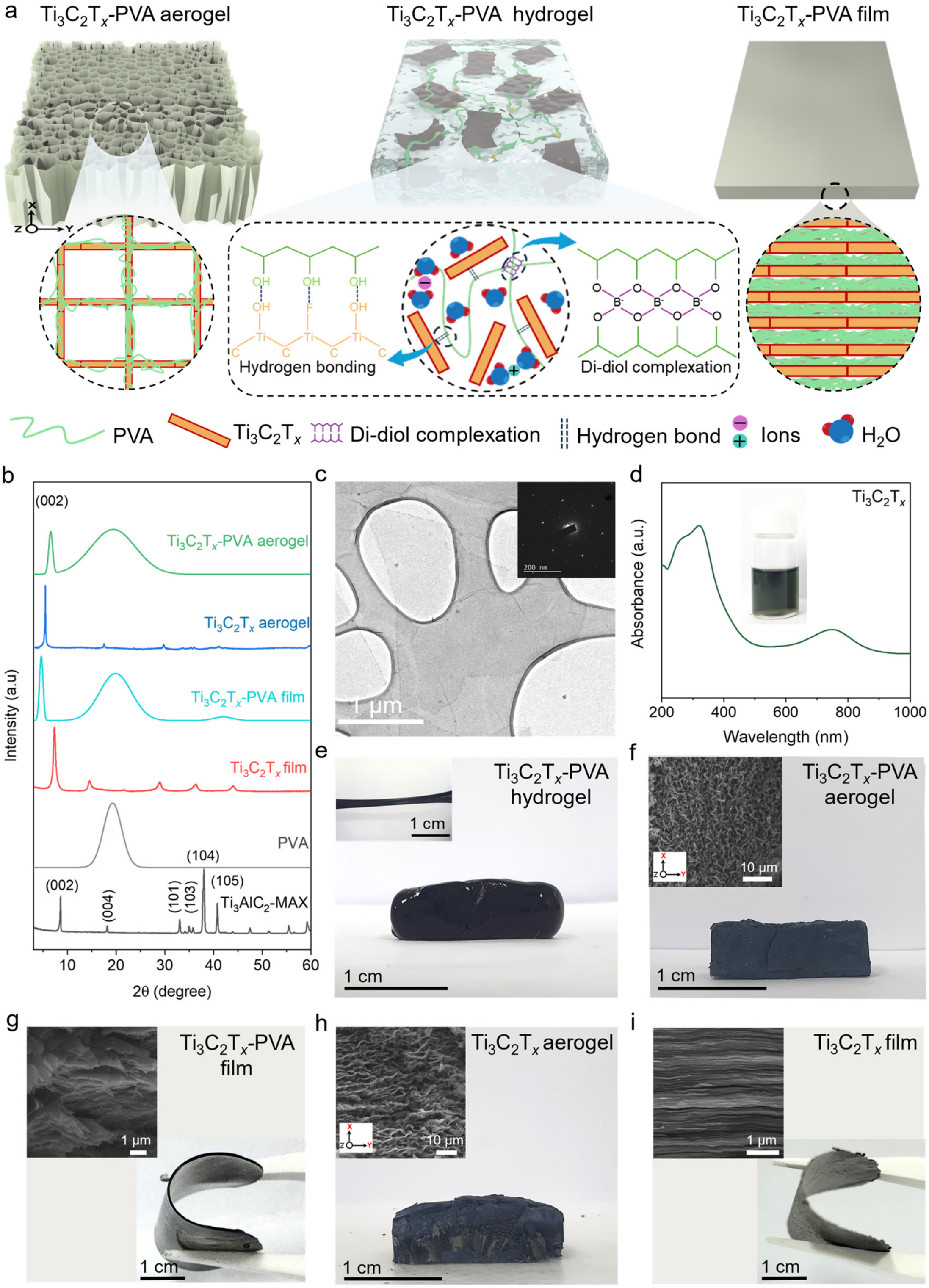

Fig. 1 (a) Schematic illustrations of $Ti_3C_2T_x$-PVA-based hydrogels, aerogels, and compact films. (b) XRD patterns of a $Ti_3C_2T_x$ compact film, $Ti_3C_2T_x$ aerogel, $Ti_3C_2T_x$-PVA compact film, and $Ti_3C_2T_x$-PVA aerogel at an areal density of 20 mg cm^{-1} and of the Ti_3AlC_2 MAX powder. (c) TEM image of a single $Ti_3C_2T_x$ sheet (inset: SAED pattern showing highly crystalline hexagonal symmetry). (d) UV-visible spectrum of $Ti_3C_2T_x$ dispersion in water (1 mg mL^{-1}). Digital photographs of (e) a $Ti_3C_2T_x$-PVA hydrogel (inset: photograph of an elongated hydrogel), (f) $Ti_3C_2T_x$-PVA aerogel (inset: SEM image), (g) $Ti_3C_2T_x$-PVA compact film (inset: SEM image), (h) $Ti_3C_2T_x$ aerogel (inset: SEM image), and (i) $Ti_3C_2T_x$ film (inset: cross-sectional SEM). All samples have the same MXene areal density of 20 mg cm^{-2}.

the remaining hydroxyl groups attached to the boron atom in the borate react with adjacent diol groups, leading to the formation of a three-dimensional elastic gel network,[37] as illustrated by the reaction equation in Fig. S2a.† The corresponding changes in bonding interactions within the hydrogel are schematically depicted in Fig. S2b and c.† This process is known as di–diol complexation and was confirmed by the presence of asymmetric stretching vibrations from the B–O–C bond at approximately 1420 cm^{-1} and 1334 cm^{-1}, as observed in Fourier-transform infrared (FTIR) spectroscopy, shown in Fig. S3.†[38,39] Ultimately, a soft and elastic hydrogel was successfully formed (Fig. 1e and its inset). For comparison, a control sample of PVA hydrogel was prepared, and it demonstrated opaque and elastic behavior, as presented in Fig. S4a–c.†

$Ti_3C_2T_x$-PVA aerogels with a uniform porous structure were produced by directionally freeze-drying $Ti_3C_2T_x$-PVA solutions (14 mg cm^{-2} to 20 mg cm^{-2}). The temperature gradient created between the copper plate and the Teflon mold facilitated the formation of a uniform porous structure (details in the Experimental section) in the *XY* direction, as shown in Fig. 1f and its inset.[40,41] Although the color shifted from white for pristine PVA to light grey and black with increasing MXene content (Fig. S5a–e†), the overall porosity and long-range order remained constant, as shown in Fig. S6a–d.†

The $Ti_3C_2T_x$-PVA compact films (Fig. S7a–e†) were fabricated by vacuum-filtering $Ti_3C_2T_x$-PVA solutions, resulting in a dense and nonporous structure (Fig. 1g and Fig. S8a–d†). Unlike the optically transparent PVA films, the $Ti_3C_2T_x$-PVA films appeared opaque (Fig. S7a–e†). For comparison, pristine $Ti_3C_2T_x$ aerogels and compact films were also fabricated from $Ti_3C_2T_x$ dispersions (Fig. 1h and i). All three $Ti_3C_2T_x$-PVA composite configurations exhibited very low density and among them, the aerogels had the lowest density, as low as 0.10 g cm^{-3} (Table S1†).

The XRD analysis of the $Ti_3C_2T_x$-PVA aerogel and compact film revealed the (002) peak characteristic of $Ti_3C_2T_x$ MXene sheets, along with a broad halo peak at approximately 20°, corresponding to the amorphous PVA peak (Fig. 1b). A slight increase in the *d*-spacing was observed compared with the $Ti_3C_2T_x$ film, which can be attributed to the intercalation of PVA into the galleries of MXene sheets. For instance, the $Ti_3C_2T_x$-PVA compact film exhibited an increased *d*-spacing of 1.56 nm compared with 1.22 nm in the $Ti_3C_2T_x$ film. In contrast, an opposite trend was detected in the $Ti_3C_2T_x$-PVA aerogel, where the *d*-spacing decreases to 1.85 nm from 1.65 nm. The reduction in *d*-spacing can be attributed to the increased compactness of the $Ti_3C_2T_x$-PVA aerogel (inset of Fig. 1f) compared to that of the $Ti_3C_2T_x$ aerogel (inset of Fig. 1h). This increased compactness is likely driven by the interfacial interactions between the hydrophilic PVA and $Ti_3C_2T_x$, which promote the formation of hydrogen bonds.[42] Additionally, the presence of anions in the system may further facilitate hydrogen bonding between $Ti_3C_2T_x$ and PVA, leading to a reduction in interlayer spacing (Fig. 1b, green spectra).[43] Note that an XRD analysis of the $Ti_3C_2T_x$-PVA hydrogels was not feasible on the Bruker D8 XRD instrument used in this study.

Mechanical properties

Mechanical properties were evaluated using a universal testing machine (Fig. 2a). The PVA hydrogel exhibited excellent stretchability, up to 450%, which can be attributed to the dynamic diol–borate crosslinking between the borax and PVA chains that effectively dissipated energy under stress (Fig. 2b). These crosslinks enhanced the hydrogel elasticity and mechanical resilience. Incorporating the $Ti_3C_2T_x$ MXene into the hydrogel further enhanced its elasticity, enabling an elongation of 636% at an areal density of 14 mg cm^{-2} (Fig. 2b) and increasing the tensile strength from 2.48 MPa to 4.83 MPa. These enhancements are ascribed to robust hydrogen bonding and diol borate complexation between the $Ti_3C_2T_x$ surface hydroxyl groups and PVA chains.[44] Specifically, the MXene surface chemistry facilitates the formation of reversible hydrogen bonding and debonding interactions with PVA, serving as a mechanism for energy absorption and distribution under stress.[45,46] The formation of hydrogen bonds can be confirmed by slight broadening of the –OH stretching peak at 3300 cm^{-1} in the $Ti_3C_2T_x$-PVA system (Fig. S3†). Additionally, the high surface area of well-delaminated $Ti_3C_2T_x$ MXenes reinforces the composite structure, enabling efficient stress transfer and contributing to improved mechanical performance. The synergistic effect of these interactions produces a mechanically resilient $Ti_3C_2T_x$-PVA hydrogel. However, further increasing the $Ti_3C_2T_x$ content to 20 mg cm^{-2} reduced elongation and fracture stress to approximately 500% and 3.44 MPa, respectively. This decrease can be attributed to impaired stretchability and increased rigidity at higher $Ti_3C_2T_x$ loadings, leading to diminished energy dissipation and the formation of stress concentration points that negatively affect the overall mechanical performance.[47,48]

Fig. 2c shows the compression resistance of the $Ti_3C_2T_x$-PVA aerogel with a $Ti_3C_2T_x$ areal density of 20 g cm^{-2}; it supported more than 1500 times its own weight without disintegrating under 30% compression. The compressive stress–strain responses of neat PVA and $Ti_3C_2T_x$-PVA aerogels are shown in Fig. 2d. Each aerogel was compressed at a displacement rate of 1.5 mm min^{-1} up to 50% strain. For the PVA aerogel, the stress barely increased until 20% strain and then gradually rose to 129 kPa at 50% strain.[49] In contrast, the $Ti_3C_2T_x$ aerogel exhibited a negligible stress response to the applied strain, indicating complete collapse under even minimal compressive strain due to its brittleness. In the $Ti_3C_2T_x$-PVA aerogels, the compressive stress increased linearly without collapse. The $Ti_3C_2T_x$-PVA aerogel at 14 mg cm^{-2} areal density achieved the highest compressive strength of 215 kPa, approximately 200 times higher than that of the $Ti_3C_2T_x$ aerogel and 50% greater than that of the PVA aerogel. However, at a higher $Ti_3C_2T_x$ areal density (20 mg cm^{-2}), the aerogel's compression stress decreased to 114 kPa. The initial compressive moduli of $Ti_3C_2T_x$-PVA aerogels at 14 mg cm^{-2} and 20 mg cm^{-2} increased by nearly 1000-fold (63 kPa) and 400-fold (24 kPa), respectively, compared with the $Ti_3C_2T_x$ aerogel (0.06 kPa) (Table S1†). Additionally, a similar trend was observed in the recovery

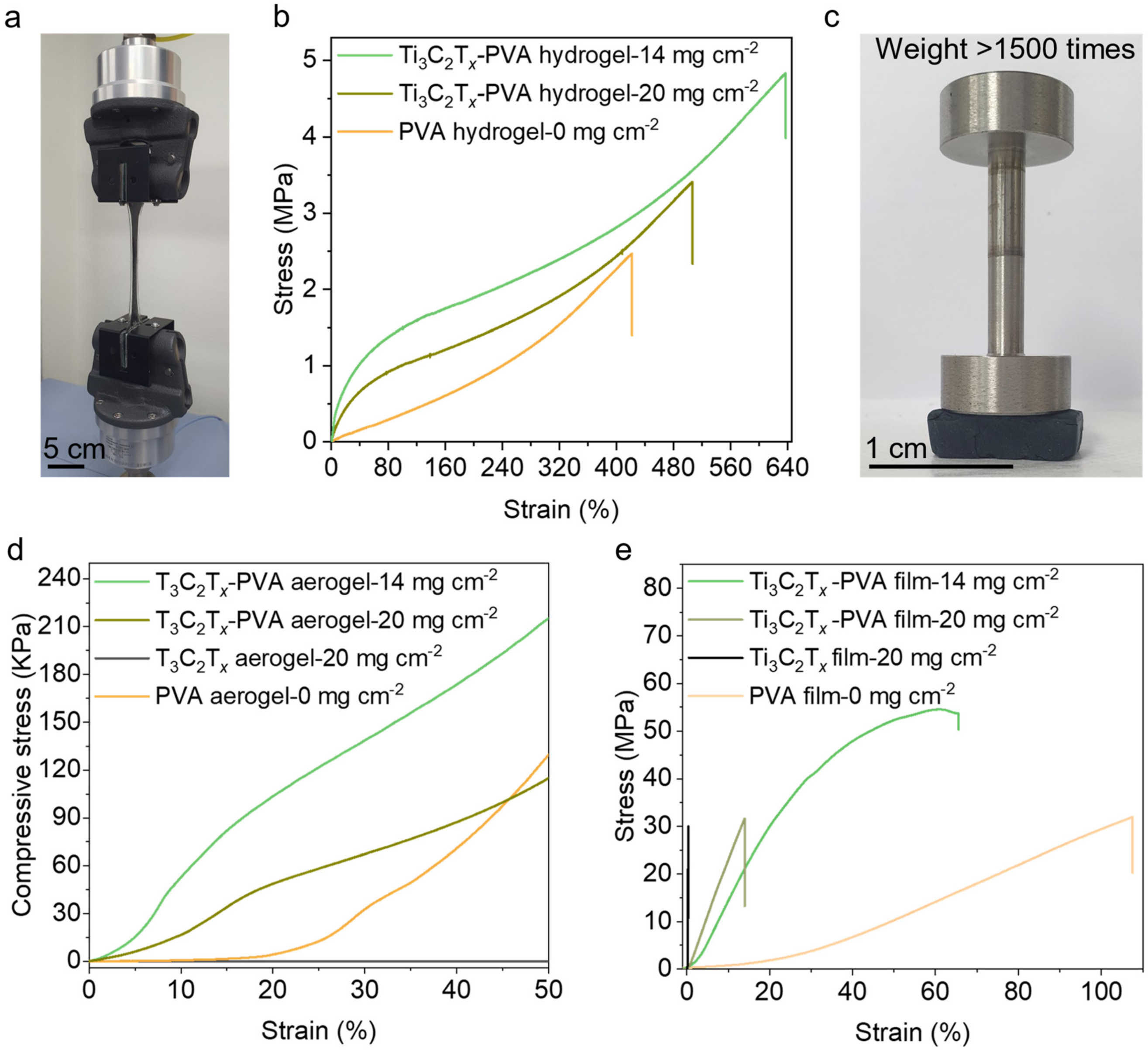

Fig. 2 (a) Digital photograph showing the tensile test of the $Ti_3C_2T_x$-PVA hydrogel. (b) Stress–strain curves of PVA and $Ti_3C_2T_x$-PVA hydrogels. (c) Digital photograph of the $Ti_3C_2T_x$-PVA aerogel supporting a load exceeding 1500 times its own weight without collapsing. (d) Stress–strain curves of PVA, $Ti_3C_2T_x$, and $Ti_3C_2T_x$-PVA aerogels at various $Ti_3C_2T_x$ areal densities. (e) Stress–strain curves of PVA, $Ti_3C_2T_x$, and $Ti_3C_2T_x$-PVA compact films at various $Ti_3C_2T_x$ areal densities.

response after removing compressive stress. The $Ti_3C_2T_x$ aerogel exhibited negligible strain recovery, almost 1%, showing poor resilience as it collapsed entirely under compression. In contrast, the PVA aerogel demonstrated a 56% strain recovery, reflecting moderate resilience. The $Ti_3C_2T_x$-PVA aerogels exhibited higher strain recovery, with around 79% and 73% for areal densities of 14 mg cm^{-2} and 20 mg cm^{-2}, respectively (Fig. S9†). This indicates significantly improved resilience, attributed to the enhanced ability of $Ti_3C_2T_x$-PVA aerogels to recover from compression without permanent deformation. The strain recovery was calculated based on the changes in the aerogel thickness before and after compression, as illustrated in Fig. S10.†

The PVA compact film exhibited substantial elongation at break (110%), with a fracture strength of 31 MPa and Young's modulus of 1.6 GPa. In contrast, the $Ti_3C_2T_x$ compact film demonstrated brittle behavior, showing only 0.6% elongation at break, a fracture strength of 29 MPa, and a notably high modulus of 9.2 GPa. Incorporating a small amount of $Ti_3C_2T_x$ (14 mg cm^{-2}) into the PVA matrix initially enhanced the mechanical properties of the $Ti_3C_2T_x$-PVA compact film, yielding a maximum fracture strength of 55 MPa almost twice that of the $Ti_3C_2T_x$ film (Fig. 2e). This enhancement is attributed to strong hydrogen-bonding interactions between $Ti_3C_2T_x$ and PVA, which promote efficient load transfer and increase the mechanical strength.[50] However, at a higher $Ti_3C_2T_x$ areal density (20 mg cm^{-2}), the ductility decreased due to disruption of the PVA matrix, which impaired efficient load transfer and resulted in brittle behavior. Consequently, the fracture stress and strain decreased to 32 MPa and 14%, respectively (Fig. 2e). Meanwhile, the Young's modulus consistently increased with the $Ti_3C_2T_x$ content, reaching 2.1 GPa at 14 mg cm^{-2} and 6.1 GPa at 20 mg cm^{-2}.

These results underscore the distinct mechanical properties of the $Ti_3C_2T_x$-PVA composites by structural form. The hydrogel demonstrated outstanding elongation (650%), the aerogel offered enhanced load-bearing capacity with a maximum compressive strength of 215 kPa, and the compact film achieved a high modulus (6.1 GPa) and good fracture strength (55 MPa). Overall, incorporating the PVA matrix significantly improved the mechanical performance of the $Ti_3C_2T_x$-PVA composites in each form compared with their pristine $Ti_3C_2T_x$ MXene counterparts.

Electrical and ionic conductivities

The structure and composition of hydrogels, aerogels, and compact films critically influence their electrical and ionic conductivities. Generally, hydrogels and dispersions exhibit high ionic conductivity due to the presence of water and ions, whereas aerogels and compact films primarily rely on electrical conductivity. In this study, $Ti_3C_2T_x$-PVA hydrogels and $Ti_3C_2T_x$ dispersions (with varying MXene areal densities ranging from 14 to 20 mg cm^{-2}) were characterized by electrochemical impedance spectroscopy at ambient temperature (Fig. 3a–c and Fig. S11a, b†). The Nyquist plots for the $Ti_3C_2T_x$-PVA hydrogels (Fig. 3a and Fig. S11a†) show a slight increase in impedance as the $Ti_3C_2T_x$ areal density increased. Conversely, in the $Ti_3C_2T_x$ dispersions (Fig. S11b†), impedance decreased as the $Ti_3C_2T_x$ areal density increased. As a result, the ionic conductivity of the $Ti_3C_2T_x$-PVA hydrogels decreased marginally with increasing MXene content, and the ionic conductivity of the $Ti_3C_2T_x$ dispersion increased (Fig. 3b and c).

In the $Ti_3C_2T_x$ dispersions, the reduction in impedance and increase in ionic conductivity (Fig. 3d) are attributed to the formation of a continuous electron-transport network by the highly conductive MXene sheets (Fig. 3e and f).[51] In contrast, gelation of the PVA matrix plays a pivotal role in the $Ti_3C_2T_x$-PVA hydrogels. The slight increase in impedance with increasing $Ti_3C_2T_x$ areal density in these hydrogels can be attributed to mobile sodium ions (Na^+) from sodium borate, which can coagulate in $Ti_3C_2T_x$ sheets (Fig. S12a and b†) and disrupt the conduction pathway.[52] Additionally, Na^+ ions can become trapped between $Ti_3C_2T_x$ layers, further hindering electron transport (Fig. 3g and h).[52,53] Nonetheless, the $Ti_3C_2T_x$-PVA hydrogels maintained relatively high ionic conductivity, likely due to the presence of ionic species within the hydrogel that facilitate ion transport.

Dielectric properties also play a significant role in EMI shielding. The real part of the permittivity (ε') of the $Ti_3C_2T_x$-PVA hydrogels measured in the X-band range (8.2–12.4 GHz) increases along with the $Ti_3C_2T_x$ areal density (Fig. 3c). This increase is primarily attributed to enhanced interfacial polarization between the $Ti_3C_2T_x$ sheets and PVA chains.[54] Additionally, polar water molecules can contribute to dielectric polarization under an electric field of electromagnetic waves.[31] Dielectric polarization is frequency-dependent, so ε' decreases with increasing frequency because the dipoles and ions have less time to align with the alternating field at high frequency.[55]

In the $Ti_3C_2T_x$-PVA aerogel and compact film, the electrical conductivity increased as the $Ti_3C_2T_x$ content increased (Fig. 3b). Although PVA is inherently insulating ($\sim 1 \times 10^{-13}$ S cm^{-1}), the high-crystallinity $Ti_3C_2T_x$ MXene is highly conductive ($\sim 1.0 \times 10^4$ S cm^{-1}). Consequently, the aerogel reached a maximum conductivity of 0.002 S cm^{-1} at the highest MXene areal density of 20 mg cm^{-2}, and the compact film attained a maximum conductivity of 0.032 S cm^{-1}. This conductivity improvement is attributed to the formation of a percolative network of conductive MXene sheets within the insulating PVA matrix, resulting in continuous conductive pathways.

The $Ti_3C_2T_x$-PVA compact film achieved significantly higher conductivity than the aerogel at the same MXene areal density, primarily due to its dense structure. $Ti_3C_2T_x$ sheets stack tightly, creating an interconnected conductive network structure that follows power-law behavior in electrical conductivity. In contrast, the aerogel's porous structure introduces large air gaps that impede electron transport, limiting its overall electrical conductivity. A similar trend was observed in $Ti_3C_2T_x$ compact film and aerogel, with compact film exhibiting higher electrical conductivity (10 000 S cm^{-1}) compared to aerogel (1.1 S cm^{-1}) as shown in Fig. 3d and Table S1.†

EMI shielding performance

The EMI shielding performance was examined at the X-band (8.2–12.4 GHz) using a waveguide measurement setup (Fig. 4a). A customized sample holder was designed to accommodate $Ti_3C_2T_x$-PVA hydrogels and $Ti_3C_2T_x$ dispersions (details in the Experimental section). The total EMI shielding effectiveness (SE_T) and its contributions from reflection (SE_R) and absorption (SE_A) were determined using eqn (2)–(8) as shown in the Experimental section below. Fig. 4b–d and Fig. S13a–f† show the X-band range EMI SE_T, SE_R, and SE_A of $Ti_3C_2T_x$-PVA hydrogels, aerogels, and compact films across various $Ti_3C_2T_x$ areal densities. To assess the influence of $Ti_3C_2T_x$ areal density on these three configurations, Fig. 4e–g present the SE_T, SE_R, and SE_A values at a midrange frequency of 10.3 GHz. These values exhibit trends similar to those of the average EMI SE_T, SE_R, and SE_A (Fig. S14a–i†). As the $Ti_3C_2T_x$ areal density increased, SE_T improved in all three configurations: hydrogel (red), aerogel (yellow), and film (blue) (Fig. 4e). Among them, the hydrogel achieved the highest EMI SE_T, followed by the film and then the aerogel. Specifically, the $Ti_3C_2T_x$-PVA hydrogel showed a gradual increase in SE_T from 41.3 dB to 66.5 dB as the $Ti_3C_2T_x$ areal density increased from 14 mg cm^{-2} to 20 mg cm^{-2}. In contrast, the $Ti_3C_2T_x$-PVA aerogel exhibited a modest increase from 1.5 dB to 2.6 dB up to 17 mg cm^{-2} before surging to 19 dB at 20 mg cm^{-2}. Meanwhile, the $Ti_3C_2T_x$-PVA compact film demonstrated a

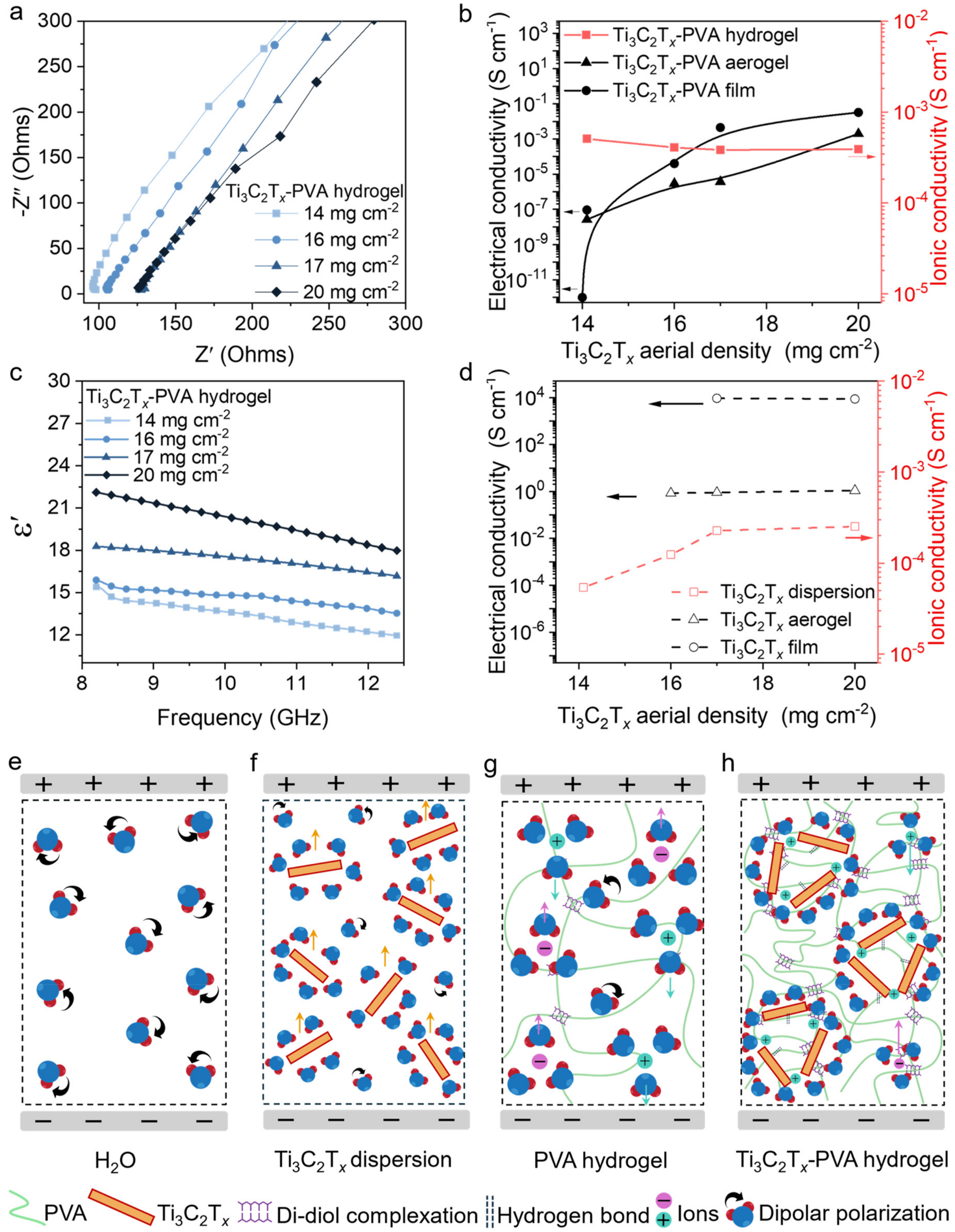

Fig. 3 (a) Nyquist impedance plots of Ti$_3$C$_2$T$_x$-PVA hydrogels at various Ti$_3$C$_2$T$_x$ areal densities. (b) Electrical conductivity of Ti$_3$C$_2$T$_x$-PVA films and aerogels and the ionic conductivity of Ti$_3$C$_2$T$_x$-PVA hydrogels plotted as a function of Ti$_3$C$_2$T$_x$ areal density. (c) Real permittivity (ε') of Ti$_3$C$_2$T$_x$-PVA hydrogels at various Ti$_3$C$_2$T$_x$ areal densities in the X-band (8.2–12.4 GHz). (d) Electrical conductivity of Ti$_3$C$_2$T$_x$ films and aerogels and ionic conductivity of Ti$_3$C$_2$T$_x$ dispersions at various Ti$_3$C$_2$T$_x$ areal densities. Schematic illustration of (e) water, (f) Ti$_3$C$_2$T$_x$, (g) PVA hydrogel, and (h) Ti$_3$C$_2$T$_x$-PVA hydrogel dispersion under an alternating electric field of electromagnetic waves.

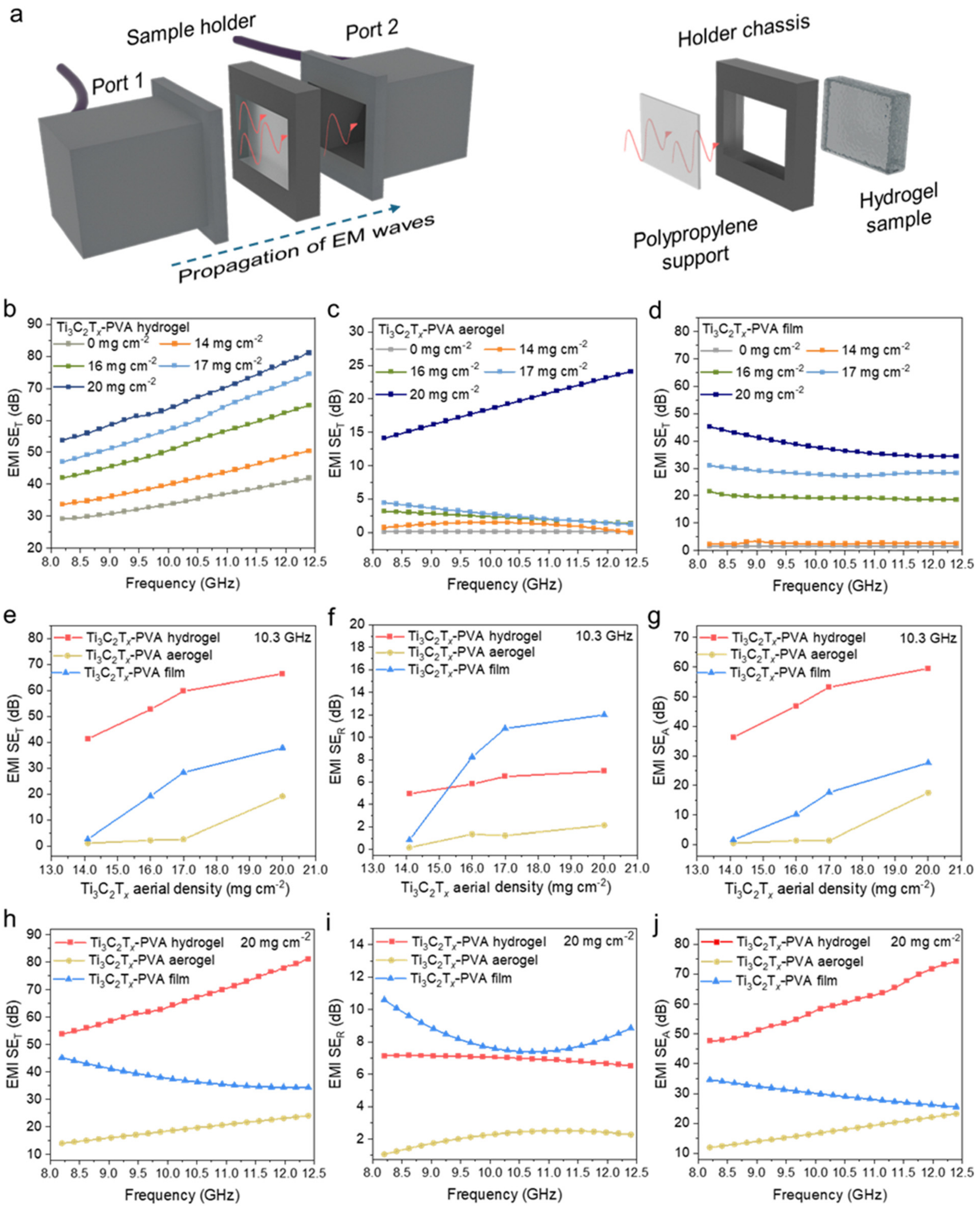

Fig. 4 (a) Schematic illustration of the customized experimental setup used to measure the EMI total shielding effectiveness (SE_T) of the hydrogels and dispersions, using a holder with a transparent polyimide film support. The EMI SE_T of the (b) $Ti_3C_2T_x$-PVA hydrogels, (c) $Ti_3C_2T_x$-PVA aerogels, and (d) $Ti_3C_2T_x$-PVA compact films as a function of $Ti_3C_2T_x$ areal density. (e) The EMI SE_T, (f) SE_R, and (g) SE_A values measured at 10.3 GHz as a function of $Ti_3C_2T_x$ areal density. (h) The EMI SE_T, (i) SE_R, and (j) SE_A values at a fixed $Ti_3C_2T_x$ areal density of 20 mg cm^{-1} for $Ti_3C_2T_x$-PVA hydrogels, aerogels, and films. Notably, the hydrogel and aerogel have the same thickness of 5 mm, whereas the compact film has a thickness of approximately 150 μm, as listed in Table S1.†

more pronounced increase in SE_T once the areal density surpassed 14 mg cm^{-2}, increasing from 2.6 dB (14 mg cm^{-2}) to 19.2 dB (16 mg cm^{-2}) and ultimately reaching 37.8 dB at 20 mg cm^{-2}.

The total EMI (SE_T) comprises both the reflection contribution (SE_R) and the absorption contribution (SE_A), as shown in Fig. 4f and Fig. 4g, respectively. As the $Ti_3C_2T_x$ areal density increased, the $Ti_3C_2T_x$-PVA hydrogel showed a moderate increase in SE_R from 4.95 dB (14 mg cm^{-2}) to 6.95 dB (20 mg cm^{-2}). The $Ti_3C_2T_x$-PVA aerogel displayed a minimal increase from 0.15 dB (14 mg cm^{-2}) to 2.12 dB (20 mg cm^{-2}). In contrast, the $Ti_3C_2T_x$-PVA compact film exhibited a sharp increase in SE_R, from 0.89 dB (14 mg cm^{-2}) to 8.23 dB (17 mg cm^{-2}), ultimately reaching 20 dB (20 mg cm^{-2}). Fig. 4g shows that SE_A is the dominant contributor to SE_T, following a trend similar to that of SE_T: the hydrogel achieved the highest EMI SE_A, followed by the film and then the aerogel. Specifically, the $Ti_3C_2T_x$-PVA hydrogel showed a gradual increase in SE_A from 36.2 dB to 59.52 (14–20 mg cm^{-2}); the aerogel SE_A remained low (0.48–1.39 dB) until 17 mg cm^{-2} and then jumped to 17.5 dB; the film SE_A steadily increased from 1.6 dB to 26.5 dB.

At a fixed areal density of 20 mg cm^{-2} (Fig. 4h–j), the $Ti_3C_2T_x$-PVA hydrogel exhibited the highest EMI SE_T, followed by the compact film and then the aerogel. SE_A followed the same trend as SE_T, with the hydrogel showing the highest value (Fig. 4j). Meanwhile, the SE_R values differed only slightly among the samples, with the compact film exhibiting the highest result (Fig. 4i).

The superior EMI shielding of the $Ti_3C_2T_x$-PVA hydrogel arises from several factors. First, the dipolar nature of water molecules promotes polarization loss. Because a water molecule has an electronegative oxygen atom (partial negative charge) and two hydrogen atoms (partial positive charge), it aligns and rotates in response to an external electric field, leading to strong attenuation of EM wave energy.[31] Second, the uniform distribution of $Ti_3C_2T_x$ sheets in the insulating PVA matrix facilitates the formation of microcapacitors in the hydrogel, where MXene sheets act as electrodes, inducing significant capacitive loss under the AC electric field of EM waves.[56] Third, mobile ions (*e.g.*, Na^+ and Br^-) generate an internally induced electric field that leads to ionic conductivity losses and can partially depolarize water molecules, further enhancing microwave absorption.[57–59] As a result, the EMI shielding performance of the $Ti_3C_2T_x$-PVA hydrogel improved as the $Ti_3C_2T_x$ areal density increased and surpassed that of the $Ti_3C_2T_x$ dispersions at the same $Ti_3C_2T_x$ areal density (Fig. S15a–c†). For instance, at 20 mg cm^{-2}, the $Ti_3C_2T_x$ dispersion achieved an SE_T of 48.6 dB (SE_A 40.9 dB), whereas the $Ti_3C_2T_x$-PVA hydrogel attained an SE_T of 66.5 dB (SE_A 59.5 dB), even though the dispersion exhibited a slightly higher SE_R (7.7 dB). Without PVA, the $Ti_3C_2T_x$ dispersion lacks the microcapacitor effect, resulting in a lower absorption coefficient (A = 0.18) and a higher reflection coefficient (R = 0.82) than those of the $Ti_3C_2T_x$-PVA hydrogel (A = 0.24, R = 0.76) (Fig. 5a and b).

The EMI shielding performance of the $Ti_3C_2T_x$-PVA aerogel is primarily based on a conductive $Ti_3C_2T_x$ network embedded within a porous PVA matrix. Although the incorporation of PVA reduced the electrical conductivity from 0.85–1.0 S cm^{-1} in the pristine $Ti_3C_2T_x$ aerogel to 2.63×10^{-8}–1.98×10 S cm^{-1} in the $Ti_3C_2T_x$-PVA aerogel, it aided in impedance matching with free space, increasing EM wave penetration and absorption. Additionally, the conductive $Ti_3C_2T_x$ network supplied abundant free electrons for reflection, and the porous structure fos-

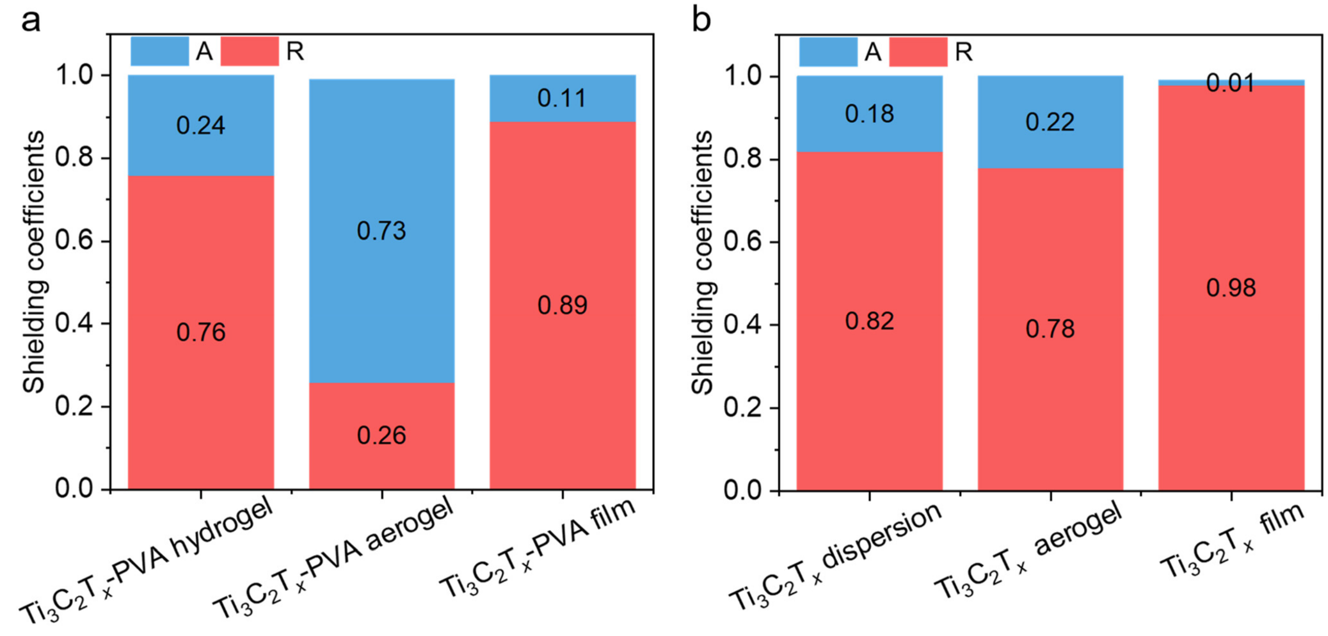

Fig. 5 Absorption coefficient (A) and reflection coefficient (R) of the (a) $Ti_3C_2T_x$-PVA-based hydrogel, aerogel, and film and (b) $Ti_3C_2T_x$-based dispersion, aerogel, and film at a fixed $Ti_3C_2T_x$ areal density (20 mg cm^{-2}).

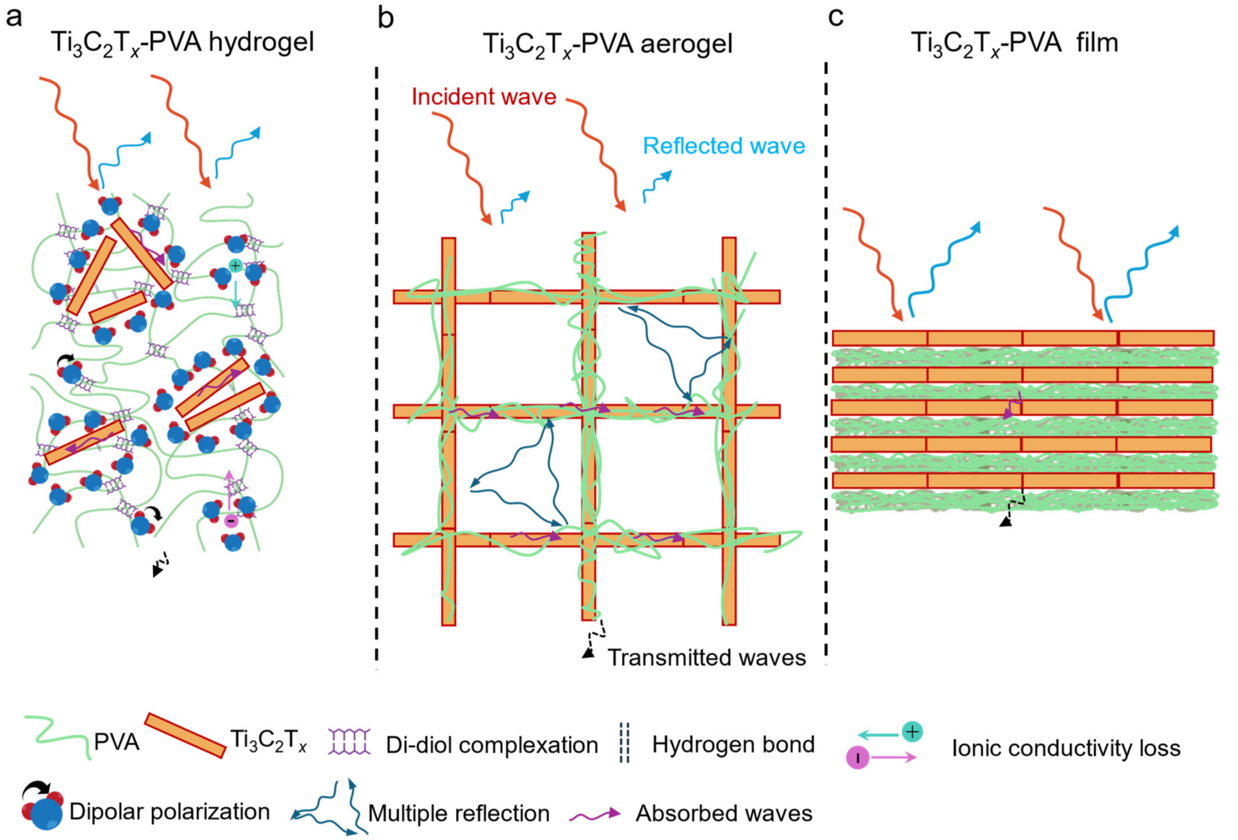

Fig. 6 Schematic illustrations of the EMI shielding mechanism in (a) $Ti_3C_2T_x$-PVA hydrogels, (b) $Ti_3C_2T_x$-PVA aerogels, and (c) $Ti_3C_2T_x$-PVA compact films. The diagrams highlight the key factors contributing to EMI shielding performance reflection, absorption, and internal multiple reflections and their respective roles in attenuating electromagnetic waves.

tered multiple internal reflections by creating numerous interfaces. As a result, although the $Ti_3C_2T_x$-PVA aerogel exhibited a slightly lower SE_T than the pristine $Ti_3C_2T_x$ aerogel at the same $Ti_3C_2T_x$ areal density (Fig. S15d–f†), it was more absorption-dominated (A ~0.73, R ~0.26 in Fig. 5a) than the pristine $Ti_3C_2T_x$ aerogel (A ~0.22, R ~0.78 in Fig. 5b) at the same areal density of 20 mg cm^{-2}.

In contrast, the $Ti_3C_2T_x$-PVA compact film primarily benefited from the dense conductive $Ti_3C_2T_x$ network within the PVA matrix, offering substantial attenuation of incident EM waves *via* reflection. The high impedance mismatch with free space limited the penetration of EM waves, and any wave that did penetrate was subsequently absorbed within the layered $Ti_3C_2T_x$-PVA structure, with reflection *via* the dominant EMI shielding mechanism, as demonstrated by the high reflection coefficient (R = 0.89) and low absorption coefficient (A = 0.11) at 20 mg cm^{-2} (Fig. 5a). As with the $Ti_3C_2T_x$-PVA aerogel, the presence of insulating PVA reduced the conductivity of the $Ti_3C_2T_x$-PVA compact film compared with the pristine $Ti_3C_2T_x$ film. Because of its high conductivity, the pristine $Ti_3C_2T_x$ film showed superior EMI shielding in the X-band (SE_T = 70 dB, SE_R = 17.5 dB, SE_A = 52.5 dB) at 20 mg cm^{-2} (Fig. S15g–i†), along with the highest reflection coefficient (R = 0.99) and lowest absorption coefficient (A = 0.01) among all configurations (Fig. 5a and b).

Fig. 6a–c illustrate the dominant shielding mechanisms for $Ti_3C_2T_x$-PVA hydrogels, aerogels, and films, respectively, with $Ti_3C_2T_x$ areal densities of 14–20 mg cm^{-2}. In the hydrogel (Fig. 6a), most incident EM waves are reflected, and those that penetrate are strongly attenuated by the robust dielectric polarization of water molecules and ions, internally induced electric fields, and efficient charge conduction through the $Ti_3C_2T_x$-PVA hydrogel, yielding the highest shielding performance. In contrast, the porous structure of the $Ti_3C_2T_x$-PVA aerogel (Fig. 6b) and its lower electrical conductivity reduced reflection but enhanced internal scattering, leading to greater absorption with minimal reflection and transmission. Meanwhile, the $Ti_3C_2T_x$-PVA compact film (Fig. 6c) exhibits reflection-dominated shielding due to its dense structure and high electrical conductivity, yielding the highest absolute specific shielding (Fig. S16†).

Conclusion

In this study, $Ti_3C_2T_x$-PVA composites were fabricated in three structural forms hydrogels, aerogels, and compact films at various $Ti_3C_2T_x$ areal densities (14–20 mg cm^{-2}) to investigate the effects of structural configuration on EMI shielding and mechanical properties. Each configuration demonstrated a distinct attenuation mechanism: hydrogels leveraged dipolar polarization, aerogels used multiple reflections and moderate conductivity, and compact films relied on dense stacking and reflection-dominated shielding. Notably, the $Ti_3C_2T_x$–PVA hydrogel achieved the highest shielding effectiveness (70 dB at 10 GHz) at a fixed $Ti_3C_2T_x$ areal density of 20 mg cm^{-2}, attributed to strong dipolar polarizations and ionic charge conduction. In contrast, the aerogel exhibited robust absorption-dominating shielding with a high absorption coefficient (A ~0.73) due to its porous architecture and enhanced multiple internal reflections. Moreover, the incorporation of PVA into $Ti_3C_2T_x$ MXenes significantly enhanced the mechanical strength across all configurations, surpassing the performance of their pristine $Ti_3C_2T_x$ MXene counterparts in all configurations. This work underscores the importance of the interplay among structural design, $Ti_3C_2T_x$ areal density, and PVA incorporation to optimize EMI shielding and mechanical performance. These findings offer insights valuable for strategically designing light-weight MXene–polymer composites in the form of hydrogels, aerogels, or compact films to enhance both EMI shielding and mechanical performance in practical applications.

Experimental section

Materials

Powders of graphite (99.8%; avg particle size, 45 μm), lithium fluoride (LiF, 98.5%), Ti (99.8%; avg particle size, 45 μm), and Al (99.8%; avg particle size, 45 μm) were purchased from Alfa Aesar. TiC powders, synthesized from a TiO_2 precursor *via* carbothermal reduction, were used to synthesize the high-crystallinity Ti_3AlC_2 MAX phase. Hydrochloric acid (HCl, 37% H_2O) and hydrofluoric acid (HF, ACS reagent grade 48 wt%) were acquired from Sigma Aldrich. Polypropylene transparent tape was purchased from 3M (ID:70005276194). Poly(vinyl alcohol) and sodium tetraborate hexahydrate (pure) were purchased from Sigma-Aldrich. All chemicals were used as received.

Synthesis of Ti_3AlC_2 MAX

The high-crystallinity Ti_3AlC_2 MAX phase was synthesized following a previously reported procedure.[35,60,61] In brief, TiC powders were mixed with Ti and an excess of Al in a molar ratio of 2 : 1.2 : 2.2, followed by ball-milling at 100 rpm for 12 h. The resulting mixture was pressed into a 50 mm diameter disk under 4000 psi and heat-treated at 1450 °C for 3 h under an argon atmosphere.[62] The resulting Ti_3AlC_2 MAX disk was pulverized and treated with 9 M HCl for 12 h to remove excess aluminum and impurities and then thoroughly rinsed with deionized water. After vacuum drying at 60 °C, the product was sieved through a 400-mesh sieve to obtain a fine, high-crystallinity Ti_3AlC_2 MAX powder suitable for subsequent $Ti_3C_2T_x$ MXene synthesis.

Synthesis of the $Ti_3C_2T_x$ MXene

The $Ti_3C_2T_x$ MXene was synthesized *via* the MILD method to selectively etch Al atoms from the parent Ti_3AlC_2 MAX phase.[3] Briefly, LiF (1.6 g) was dissolved in a mixture of 20 mL of 9 M HCl and 4 mL of 48 wt% HF in a polypropylene container. The Ti_3AlC_2 MAX powder (1 g) was gradually added to the LiF/HCl solution under continuous stirring with a magnetic stirrer at 320 rpm. The etching process was carried out for 24 h at 35 °C under continuous stirring. The resulting product was washed multiple times with deionized water by centrifuging at 5000 rpm for 5 min until the supernatant reached pH 6. The delaminated $Ti_3C_2T_x$ flakes obtained were subsequently used to prepare a 10 mg mL^{-1} $Ti_3C_2T_x$ dispersion.

Fabrication of $Ti_3C_2T_x$ PVA hydrogels, aerogels, and films

To prepare the $Ti_3C_2T_x$-PVA hydrogels, PVA solution was prepared by first dissolving 3 g of PVA in 60 mL of deionized water at 90 °C with stirring (100 rpm) for 1 hour. Predetermined amounts of $Ti_3C_2T_x$, corresponding to different $Ti_3C_2T_x$ areal densities (14, 16, 17, and 20 mg cm^{-2}), were added to 3 mL of the cooled PVA solution to form a homogeneous mixture. Subsequently, 2 mL of a 0.026 M sodium tetraborate decahydrate solution was added dropwise, and the mixture was gently stirred until gelation occurred. Borate ions interact with the hydroxyl groups of PVA *via* hydrogen bonding and di-diol borate complexation, forming an elastic gel network. The resulting 5 mm thick $Ti_3C_2T_x$-PVA hydrogels with various $Ti_3C_2T_x$ areal densities were used for further experiments. The $Ti_3C_2T_x$-PVA aerogels were obtained by freezing the $Ti_3C_2T_x$-PVA solution (with the predetermined $Ti_3C_2T_x$ areal density) using directional freezing at −110 °C and 0.1 Pa for 48 hours. The solution was poured into a Teflon mold (23 mm × 11 mm × 45 mm) equipped with a copper plate. The Teflon mold provided thermal insulation, and the copper plate provided a temperature gradient. Similarly, the compact $Ti_3C_2T_x$-PVA films were fabricated by vacuum-filtering $Ti_3C_2T_x$-PVA solutions (with the predetermined $Ti_3C_2T_x$ areal density) under ambient conditions. As control samples, PVA hydrogels, aerogels, and compact films were prepared following the same procedures, but without $Ti_3C_2T_x$.

Fabrication of $Ti_3C_2T_x$ dispersions, aerogels, and films

$Ti_3C_2T_x$ dispersions with various MXene areal densities (14–20 mg cm^{-2}) were prepared from a 10 mg mL^{-1} stock solution by diluting with deionized water. The $Ti_3C_2T_x$ hydrogels, aerogels, and compact films were prepared from $Ti_3C_2T_x$ dispersions at predetermined MXene areal densities following the same procedures used for the $Ti_3C_2T_x$-PVA hydrogels, aerogels, and films but without adding PVA.

Material characterization

The surface and cross-sectional morphologies of the MXene flakes and nanocomposites were examined using a field-emission SEM (JSM-7600F, Japan) equipped with an EDS system. The crystal structure was investigated using XRD (D8, Bruker, USA) with Cu Kα radiation. The XRD scans spanned a 2θ range of 4°–80° at a rate of 2° min^{-1} and a window slit dimension of 10 × 10 mm^2. High-resolution TEM (JEM-2100F, Japan) at an acceleration voltage of 200 kV was used for the atomic-scale structural analysis of individual $Ti_3C_2T_x$ flakes. Electrical conductivity measurements were performed using a four-point probe (MCP-TP06P PSP) connected to a Loresta-GP meter (Model MCP-T610, Mitsubishi Chemical, Japan).

Measurements

Tensile and compression testing. Uniaxial tensile mechanical tests were performed under ambient conditions using a universal testing machine (Shimadzu AGS-X) equipped with a 2 KN load cell and a crosshead speed of 1 mm min^{-1}. The sample dimensions were 30 mm × 10 mm × ∼200 µm (length × width × thickness). A paper support was used in the $Ti_3C_2T_x$ films, and a tape support was used for hydrogels. Compression tests were carried out with a 2K N load cell at a displacement rate of 1.5 mm min^{-1}. The strain recovery was calculated using the changes in thickness of the aerogel before and after compressive stress.

Ionic conductivity. The ionic conductivities (σ_i) of the hydrogels and dispersions in the relaxed state were determined by AC impedance spectroscopy using an electrochemical workstation system (CHI660E) with a three-electrode setup. The voltage amplitude was set to 10 mV, and the frequency was swept from 100 kHz to 0.01 Hz. Each hydrogel sample was placed between two stainless-steel plate electrodes. The ionic resistance was obtained by extrapolating the impedance curve to the x-axis, and ionic conductivity was calculated according to eqn (1).[63]

$$\sigma_i = \frac{L}{(A \times R)} \tag{1}$$

where σ_i is the ionic conductivity, L is the distance between two electrodes, A is the electrode surface area, and R is the resistance.

Permittivity and EMI shielding. EMI-shielding measurements were performed over the X-band (8.2–12.4 GHz) using a two-port vector network analyzer (VNA, N5222B, Keysight, USA) coupled with a rectangular waveguide. A custom sample holder, with inner dimensions of 23 mm × 11 mm × 10 mm, was designed for both the dispersions and hydrogels. After the hydrogel sample was placed into the holder chassis, a transparent polyimide support sealed the holder to prevent any hydrogel leakage.

The permittivity of the dispersions and hydrogels was calculated in a similar manner, with calibration performed based on air, short-circuit, and deionized water measurements at room temperature prior to the actual measurements. The complex relative permittivity (ε_r) is given by eqn (2).

$$\varepsilon_r = \varepsilon' - j\varepsilon'' \tag{2}$$

where ε' (the real part) represents the dielectric constant and ε'' (the imaginary part) represents a loss factor.

The scattering parameters (S_{mn}), including S_{11}, S_{22}, S_{21}, and S_{12}, were obtained using the two-port VNA. The subscripts m and n represent the transmitting and receiving ports, respectively. R and T can be calculated using the respective eqn (4) and (5).

$$S_{12} = \frac{V_{1(\text{output})}}{V_{2(\text{input})}} = \frac{E_{1(\text{output})}}{E_{2(\text{input})}} \tag{3}$$

$$R = \frac{P_r}{P_i} = |S_{11}|^2 = |S_{22}|^2 \tag{4}$$

$$T = \frac{P_t}{P_i} = |S_{12}|^2 = |S_{21}|^2 \tag{5}$$

$$SE_T = 10 \log \frac{1}{T} \tag{6}$$

$$SE_R = 10 \log \frac{1}{1-R} \tag{7}$$

$$SE_A = 10 \log \frac{1-R}{T} \tag{8}$$

The total shielding effectiveness (SE_T) of a material at a given single impedance was calculated as the combined effects of reflection (SE_R) and absorption (SE_A).

$$SE_T = SE_R + SE_A \tag{9}$$

Author contributions

S.M.N. and C.M.K. conceived the idea. S.M.N. designed and conducted the experiments. S.M.N., T.H., A.I., S.Z., S.C., N.H., X.K., Z.K., Z.H., and C.M.K. discussed the results and analyzed the data. S.M.N. and C.M.K. authored the manuscript with input from all the authors. C.M.K. supervised the study.

Data availability

The authors confirm that the data supporting the findings of this study are available within the article and its ESI.†

Conflicts of interest

The authors declare no conflicts of interest.

Acknowledgements

This study was supported by grants from the Basic Science Research Program (2021M3H4A1A03047327 and 2022R1A2C3006227) through the National Research Foundation of Korea, funded by the Ministry of Science, ICT, and Future Planning, Republic of Korea; and the National Research Council of Science & Technology (NST), funded by the Korean Government (MSIT) (CRC22031-000). This research was partially supported by the Ministry of Trade, Industry, and

Energy (MOTIE) and the Korean Institute for Advancement of Technology (KIAT) through the International Cooperative R&D program (P0028332). This study was partially supported by a grant from Hyundai Mobis.

References

1 D. D. L. Chung, *Carbon*, 2001, **39**, 279–285.

2 P. Kumar, F. Shahzad, S. Yu, S. M. Hong, Y.-H. Kim and C. M. Koo, *Carbon*, 2015, **94**, 494–500.

3 S. K. Hong, K. Y. Kim, T. Y. Kim, J. H. Kim, S. W. Park, J. H. Kim and B. J. Cho, *Nanotechnology*, 2012, **23**, 455704.

4 L. De Temmerman, *J. Coated Fabr.*, 1992, **21**, 191–198.

5 S. H. Lee, S. Yu, F. Shahzad, J. Hong, S. J. Noh, W. N. Kim, S. M. Hong and C. M. J. C. S. Koo and Technology, *Compos. Sci. Technol.*, 2019, **182**, 107778.

6 Y.-S. Choi, Y.-H. Yoo, J.-G. Kim, S.-H. J. S. Kim and C. Technology, *Surf. Coat. Technol.*, 2006, **201**, 3775–3782.

7 M.-S. Cao, X.-X. Wang, W.-Q. Cao and J. Yuan, *J. Mater. Chem. C*, 2015, **3**, 6589–6599.

8 J.-M. Thomassin, C. Jérôme, T. Pardoen, C. Bailly, I. Huynen and C. Detrembleur, *Mater. Sci. Eng., R*, 2013, **74**, 211–232.

9 M. H. Al-Saleh and U. Sundararaj, *Carbon*, 2009, **47**, 1738–1746.

10 C. Pavlou, M. G. Pastore Carbone, A. C. Manikas, G. Trakakis, C. Koral, G. Papari, A. Andreone and C. Galiotis, *Nat. Commun.*, 2021, **12**, 4655.

11 H. Wang, X. Sun, Y. Wang, K. Li, J. Wang, X. Dai, B. Chen, D. Chong, L. Zhang and J. Yan, *Nat. Commun.*, 2023, **14**, 380.

12 A. S. Zeraati, S. A. Mirkhani, P. Sun, M. Naguib, P. V. Braun and U. Sundararaj, *Nanoscale*, 2021, **13**, 3572–3580.

13 X. Li, Z. Huang, C. E. Shuck, G. Liang, Y. Gogotsi and C. Zhi, *Nat. Rev. Chem.*, 2022, **6**, 389–404.

14 S. Abdolhosseinzadeh, X. Jiang, H. Zhang, J. Qiu and C. Zhang, *Mater. Today*, 2021, **48**, 214–240.

15 F. Shahzad, M. Alhabeb, C. B. Hatter, B. Anasori, S. Man Hong, C. M. Koo and Y. Gogotsi, *Science*, 2016, **353**, 1137–1140.

16 A. Iqbal, F. Shahzad, K. Hantanasirisakul, M.-K. Kim, J. Kwon, J. Hong, H. Kim, D. Kim, Y. Gogotsi and C. M. Koo, *Science*, 2020, **369**, 446–450.

17 R. Yan, Q. Lin, K. You, L. Zhang, Y. Chen, Z. Huang and X. Sheng, *Soft Sci.*, 2025, **5**, 8.

18 L.-X. Liu, W. Chen, H.-B. Zhang, L. Ye, Z. Wang, Y. Zhang, P. Min and Z.-Z. Yu, *Nano-Micro Lett.*, 2022, **14**, 111.

19 J.-Q. Luo, S. Zhao, H.-B. Zhang, Z. Deng, L. Li and Z.-Z. Yu, *Compos. Sci. Technol.*, 2019, **182**, 107754.

20 T. Tang, S. Wang, Y. Jiang, Z. Xu, Y. Chen, T. Peng, F. Khan, J. Feng, P. Song and Y. Zhao, *J. Mater. Sci. Technol.*, 2022, **111**, 66–75.

21 Q. Gao, Y. Pan, G. Zheng, C. Liu, C. Shen and X. Liu, *Adv. Compos. Hybrid Mater.*, 2021, **4**, 274–285.

22 F. Jia, J. Dong, X. Dai, Y. Liu, H. Wang and Z. Lu, *Chem. Eng. J.*, 2023, **452**, 139395.

23 X. Wu, B. Han, H.-B. Zhang, X. Xie, T. Tu, Y. Zhang, Y. Dai, R. Yang and Z.-Z. Yu, *Chem. Eng. J.*, 2020, **381**, 122622.

24 S. Habibpour, K. Zarshenas, M. Zhang, M. Hamidinejad, L. Ma, C. B. Park and A. Yu, *ACS Appl. Mater. Interfaces*, 2022, **14**, 21521–21534.

25 G. M. Weng, J. Li, M. Alhabeb, C. Karpovich, H. Wang, J. Lipton, K. Maleski, J. Kong, E. Shaulsky and M. Elimelech, *Adv. Funct. Mater.*, 2018, **28**, 1803360.

26 Y. Zhang, K. Ruan, K. Zhou and J. Gu, *Adv. Mater.*, 2023, **35**, 2211642.

27 J. Dong, Z. Li, C. Liu, B. Zhou, C. Liu and Y. Feng, *Nano Res.*, 2024, **17**, 5651–5660.

28 H. Xu, X. Yin, X. Li, M. Li, S. Liang, L. Zhang and L. Cheng, *ACS Appl. Mater. Interfaces*, 2019, **11**, 10198–10207.

29 Y. Cheng, X. Li, Y. Qin, Y. Fang, G. Liu, Z. Wang, J. Matz, P. Dong, J. Shen and M. Ye, *Sci. Adv.*, 2021, **7**, eabj1663.

30 E. Kim, H. Zhang, J.-H. Lee, H. Chen, H. Zhang, M. H. Javed, X. Shen and J.-K. Kim, *Composites, Part A*, 2021, **147**, 106430.

31 J. Hong, J. Kwon, A. Iqbal, D. Kim, T. Kwon, P. Sambyal, S. M. Hong, H. G. Yoon, M.-K. Kim and C. M. Koo, *Chem. Eng. J.*, 2022, **438**, 135564.

32 J. Liu, L. Mckeon, J. Garcia, S. Pinilla, S. Barwich, M. Möbius, P. Stamenov, J. N. Coleman and V. Nicolosi, *Adv. Mater.*, 2022, **34**, 2106253.

33 Y. Yang, N. Wu, B. Li, W. Liu, F. Pan, Z. Zeng and J. Liu, *ACS Nano*, 2022, **16**, 15042–15052.

34 Y. Yang, B. Li, N. Wu, W. Liu, S. Zhao, C. J. Zhang, J. Liu and Z. Zeng, *ACS Mater. Lett.*, 2022, **4**, 2352–2361.

35 A. Iqbal, J. Kwon, T. Hassan, S. W. Park, W.-H. Lee, J.-M. Oh, J. Hong, J. Lee, S. M. Naqvi, U. Zafar, S. J. Kim, J. H. Park, M.-K. Kim and C. M. Koo, *Adv. Funct. Mater.*, 2024, 2409346.

36 M. Ghidiu and M. W. Barsoum, *J. Am. Ceram. Soc.*, 2017, **100**, 5395–5399.

37 M. B. Lawrence, J. A. E. Desa and V. K. Aswal, *Mater. Res. Express*, 2018, **5**, 015315.

38 J. Han, H. Wang, Y. Yue, C. Mei, J. Chen, C. Huang, Q. Wu and X. Xu, *Carbon*, 2019, **149**, 1–18.

39 E. Al-Emam, H. Soenen, J. Caen and K. Janssens, *Heritage Sci.*, 2020, **8**, 106.

40 P. Sambyal, A. Iqbal, J. Hong, H. Kim, M.-K. Kim, S. M. Hong, M. Han, Y. Gogotsi and C. M. Koo, *ACS Appl. Mater. Interfaces*, 2019, **11**, 38046–38054.

41 M. Han, X. Yin, K. Hantanasirisakul, X. Li, A. Iqbal, C. B. Hatter, B. Anasori, C. M. Koo, T. Torita, Y. Soda, L. Zhang, L. Cheng and Y. Gogotsi, *Adv. Opt. Mater.*, 2019, **7**, 1900267.

42 Z.-Y. Sui, Q.-H. Meng, J.-T. Li, J.-H. Zhu, Y. Cui and B.-H. Han, *J. Mater. Chem. A*, 2014, **2**, 9891–9898.

43 C. Cai, L. Zhang, X. Meng, B. Luo, Y. Liu, M. Chi, J. Wang, T. Liu, S. Zhang, S. Wang and S. Nie, *Nano Lett.*, 2024, **24**, 16022–16030.

44 J. Liu and V. Nicolosi, *Adv. Funct. Mater.*, 2024, 2407439.

45 Y. Lu, X. Qu, W. Zhao, Y. Ren, W. Si, W. Wang, Q. Wang, W. Huang and X. Dong, *Am. Assoc. Adv. Sci.*, 2020, **2020**, 2038560.

46 J. Zhang, L. Wan, Y. Gao, X. Fang, T. Lu, L. Pan and F. Xuan, *Adv. Electron. Mater.*, 2019, **5**, 1900285.

47 H. Liu, C. Du, L. Liao, H. Zhang, H. Zhou, W. Zhou, T. Ren, Z. Sun, Y. Lu, Z. Nie, F. Xu, J. Zhu and W. Huang, *Nat. Commun.*, 2022, **13**, 3420.

48 S. Zhang, F. Guo, X. Gao, M. Yang, X. Huang, D. Zhang, X. Li, Y. Zhang, Y. Shang and A. Cao, *Adv. Sci.*, 2024, **11**, 2405880.

49 Z. Zhou, N. Zheng and W. Sun, *Carbon*, 2023, **201**, 60–70.

50 Z. Ling, C. E. Ren, M.-Q. Zhao, J. Yang, J. M. Giammarco, J. Qiu, M. W. Barsoum and Y. Gogotsi, *Proc. Natl. Acad. Sci. U. S. A.*, 2014, **111**, 16676–16681.

51 M. Lounasvuori, T. Zhang, Y. Gogotsi and T. Petit, *J. Phys. Chem. C*, 2024, **128**, 2803–2813.

52 Y. Deng, T. Shang, Z. Wu, Y. Tao, C. Luo, J. Liang, D. Han, R. Lyu, C. Qi, W. Lv, F. Kang and Q.-H. Yang, *Adv. Mater.*, 2019, **31**, 1902432.

53 L. Zhao, L. Bi, J. Hu, G. Gao, D. Zhang, Y. Li, A. Flynn, T. Zhang, R. Wang, X. M. Cheng, L. Liu, Y. Gogotsi and B. Li, *Nat. Commun.*, 2024, **15**, 10027.

54 W. Wan, M. Tao, H. Cao, Y. Zhao, J. Luo, J. Yang and T. Qiu, *Ceram. Int.*, 2020, **46**, 13862–13868.

55 M. E. Londoño, J. M. Jaramillo, R. Sabater and J. M. Vélez, *Rev. EIA*, 2012, 105–114.

56 A. Iqbal, P. Sambyal, J. Kwon, M. Han, J. Hong, S. J. Kim, M.-K. Kim, Y. Gogotsi and C. M. Koo, *Compos. Sci. Technol.*, 2021, **213**, 108878.

57 N. Gavish and K. Promislow, *Phys. Rev. E*, 2016, **94**, 012611.

58 N. Q. Vinh, M. S. Sherwin, S. J. Allen, D. K. George, A. J. Rahmani and K. W. Plaxco, *J. Chem. Phys.*, 2015, **142**, 164502.

59 A. Iqbal, T. Hassan, S. M. Naqvi, Y. Gogotsi and C. M. Koo, *Nat. Rev. Electr. Eng.*, 2024, **1**, 180–198.

60 T. S. Mathis, K. Maleski, A. Goad, A. Sarycheva, M. Anayee, A. C. Foucher, K. Hantanasirisakul, C. E. Shuck, E. A. Stach and Y. Gogotsi, *ACS Nano*, 2021, **15**, 6420–6429.

61 T. Hassan, A. Iqbal, B. Yoo, J. Y. Jo, N. Cakmakci, S. M. Naqvi, H. Kim, S. Jung, N. Hussain, U. Zafar, S. Y. Cho, S. Jeong, J. Kim, J. M. Oh, S. Park, Y. Jeong and C. M. Koo, *Nano-Micro Lett.*, 2024, **16**, 216.

62 A. Iqbal, H. Kim, J. M. Oh, J. Chae, J. Kim, M. Kim, T. Hassan, Z. Gao, J. Lee and S. J. Kim, *Small methods*, 2023, **7**, 2201715.

63 H. Cheng, X. He, Z. Fan and J. Ouyang, *Adv. Energy Mater.*, 2019, **9**, 1901085.